

Article

Calculation for High Pressure Behaviour of Potential Solar Cell Materials $\text{Cu}_2\text{FeSnS}_4$ and $\text{Cu}_2\text{MnSnS}_4$

Tim Küllmey ^{1,*}, Miguel González ¹, Eva M. Heppke ² and Beate Paulus ¹

¹ Institut für Chemie und Biochemie, Freie Universität Berlin, Arnimallee 22, 14195 Berlin, Germany; gonzalem92@zedat.fu-berlin.de (M.G.); b.paulus@fu-berlin.de (B.P.)

² Institut für Chemie, Technische Universität Berlin, Strasse des 17. Juni 135, 10623 Berlin, Germany; e.heppke@tu-berlin.de

* Correspondence: tim.kuellmey@fu-berlin.de

Abstract: Exploring alternatives to the $\text{Cu}_2\text{ZnSnS}_4$ kesterite solar cell absorber, we have calculated first principle enthalpies of different plausible structural models (kesterite, stannite, $P\bar{4}$ and GeSb type) for $\text{Cu}_2\text{FeSnS}_4$ and $\text{Cu}_2\text{MnSnS}_4$ to identify low and high pressure phases. Due to the magnetic nature of Fe and Mn atoms we included a ferromagnetic (FM) and anti-ferromagnetic (AM) phase for each structural model. For $\text{Cu}_2\text{FeSnS}_4$ we predict the following transitions: $P\bar{4}$ (AM) $\xrightarrow{16.3 \text{ GPa}}$ GeSb type (AM) $\xrightarrow{23.0 \text{ GPa}}$ GeSb type (FM). At the first transition the electronic structure changes from semi-conducting to metallic and remains metallic throughout the second transition. For $\text{Cu}_2\text{MnSnS}_4$, we predict a direct AM (kesterite) to FM (GeSb-type) transitions at somewhat lower pressure (12.1 GPa). The GeSb-type structure also shows metallic behaviour.

Keywords: DFT; magnetic materials; solar cell absorber; kesterite; high pressure



Citation: Küllmey, T.; González, M.; Heppke, E.M.; Paulus, B. Calculation for High Pressure Behaviour of Potential Solar Cell Materials $\text{Cu}_2\text{FeSnS}_4$ and $\text{Cu}_2\text{MnSnS}_4$. *Crystals* **2021**, *11*, 151. <https://doi.org/10.3390/cryst11020151>

Academic Editor: Sławomir J. Grabowski
Received: 8 January 2021
Accepted: 27 January 2021
Published: 2 February 2021

Publisher's Note: MDPI stays neutral with regard to jurisdictional claims in published maps and institutional affiliations.



Copyright: © 2020 by the authors. Licensee MDPI, Basel, Switzerland. This article is an open access article distributed under the terms and conditions of the Creative Commons Attribution (CC BY) license (<https://creativecommons.org/licenses/by/4.0/>).

1. Introduction

The impending exhaustion of fossil fuel has prompted the exploration and exploitation of alternative energy resources, with the solar energy harvesting through photovoltaic devices spearheading these efforts. In an attempt to overcome the restraints of Si-based materials, the direct optical band gap of chalcogenide-based solar cells offers the benefit of higher absorption in comparison to silicon. Given that the employed chalcogenides are composed of multiple elements, one can additionally optimise the photovoltaic properties of the respective material by appropriate metal or chalcogenide substitution. Among the various chalcogenides investigated for this purpose, the quaternary semiconductor $\text{Cu}_2\text{ZnSnS}_4$ has attracted considerable attention [1,2]. The suitability of this material for solar cell applications stems from its almost optimal band gap ($E_g \approx 1.5 \text{ eV}$), its high absorption coefficient in the visible range, and its earth-abundant, low-cost, and non-toxic constituents [3–5]. In a previous experimental and theoretical study on $\text{Cu}_2\text{ZnSnS}_4$ we have investigated the high pressure behaviour to probe its reaction to tensile stress [6]. One of the biggest issues with $\text{Cu}_2\text{ZnSnS}_4$ is that it suffers from Cu-Zn cationic disorder [7]. The main reason why Cu and Zn can be interchanged easily is their similar ionic radius. The analogues $\text{Cu}_2\text{FeSnS}_4$ and $\text{Cu}_2\text{MnSnS}_4$ have similarly favourable properties for use as a solar cell absorber. We expect cationic disorder to be less present due to the bigger difference in size of Fe and Mn in comparison to Cu. In this work, we want use density functional-based (DFT) first principle methods to investigate how $\text{Cu}_2\text{FeSnS}_4$ and $\text{Cu}_2\text{MnSnS}_4$ behave under tensile stress to understand the physical limitation of those materials.

2. Materials and Methods

2.1. Calculation Set-Up

The periodic density functional theory (DFT) calculations were performed with VASP 5.4.4 [8–11]. A plane wave basis set with an energy cutoff of 550 eV with the projector

augmented (PAW) potentials [12,13] was used, whereby the 5s, 5p and 4d electrons of Sn, 3s, 3p electrons of S, and 4s, 3d electrons of Cu, Fe and Mn were explicitly considered. The electronic convergence criteria was set at least to 10^{-5} eV, whereby the Blocked-Davidson algorithm was applied as implemented in VASP. The structural relaxation of internal and external lattice parameters was set to a force convergence of 10^{-2} eV/Å² while the conjugate-gradient algorithm implemented in VASP was used [14]. The freedom of spin polarisation was enabled and a Gaussian smearing approach with a smearing factor σ of 0.01 eV was utilised. For all structures we simulated 16 atoms which corresponds to the number of atoms in the kesterite unit cell. The cells were fully optimised with a $8 \times 8 \times 4$ k-grid constructed via the Monkhorst-Pack scheme [15] and centered at the Γ -point with the PBE functional [16]. The cells include two magnetic ions (Fe or Mn) which can be arranged in two different magnetic phases, ferromagnetic (FM) with parallel magnetic moments and anti-ferromagnetic (AM) with antiparallel ones. On top of the PBE-optimised structures, single point calculations for the band gap and DOS with the HSE06-functional [17–20] were performed with a $4 \times 4 \times 2$ k-grid to account for an accurate electronic structure. The tetrahedron method with Blöchl corrections [21] was applied for band structure evaluation.

The pressure dependence was determined by selecting volume points in a range of about 50 Å³ below the minima. This corresponds to a pressure range of 0–30 GPa. We used a step size of 8 Å³ which lead to at least 10 volume points for each structural model. At each point we optimised the ionic positions and cell shape, while keeping the volume constant. We fitted the total energy versus volume to a Birch-Murnaghan Equation of State (B-M EoS) [22]. Then the pressure at each volume was obtained from the $P(V)$ formulation of the same EoS (for details see Appendix A.3). Using the pressure we calculated the enthalpies ($H(P) = E + PV$) for each structural model and compared them over the investigated pressure range to identify the most stable structures.

All energy and enthalpy differences between different structural models in the following refer to the KS unit cell size, hence to two formula units.

2.2. Structural Models

In quaternary chalcogenide semiconductors the equilibrium structure at ambient pressures in most cases are kesterite (KS, Figure 1a) or stannite (ST, Figure 1b) structures [23,24]. We include both structures as potential low pressure phases for Cu₂FeSnS₄ and Cu₂MnSnS₄. Please note that in the cited work by Schorr et al. [23] besides KS and ST also three disordered structures are suggested which are very unlikely to occur in our systems due to the different ionic radii of the involved elements. In our high pressure study on Cu₂ZnSnS₄ we found the distorted rocksalt structure (GeSb, Figure 1c) to be the most stable phase beyond 16 GPa [6]. Therefore we include GeSb as a high pressure phase in this study. We also include a tetragonal $P\bar{4}$ structure (Figure 1d), which is discussed in literature as the thermodynamically most stable structure for Cu₂FeSnS₄ [25–27].

KS, ST and $P\bar{4}$ have a coordination number of 4, due to the same structural motif, they are close in formation energy and which structure forms depends on the crystallisation conditions. Unless the crystallisation is done carefully to enable the formation of the thermodynamic equilibrium the crystallisation process is kinetically driven, which we can not simulate in our DFT calculations. The high pressure phase GeSb has a coordination number of 6. Transitioning from a four to a six-fold coordination is a massive structural change associated with a large difference in the energy of formation. Due to the large energy difference, we can describe the pressure induced transition well in DFT.

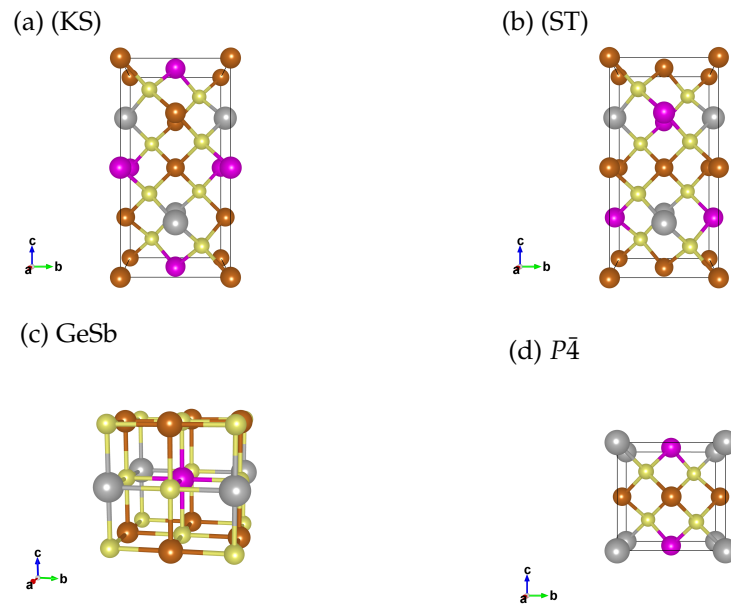


Figure 1. Structural models for the unit cell of (a) Kesterite (KS, $I\bar{4}$), (b) Stannite (ST, $I\bar{4}2m$), (c) GeSb ($P4/mmm$) and (d) $P\bar{4}$ structure. Bronze: Cu, pink: Fe/Mn, grey: Sn and yellow: S. For the GeSb and the $P\bar{4}$ structure we utilise two unit cells (stacked along the c axis), so that the number of atoms matches the KS/ST unit cell we use in the calculation.

3. Results and Discussion

3.1. Equilibrium Structures

Before discussing the enthalpies we will review the equilibrium structures at zero pressure of $\text{Cu}_2\text{FeSnS}_4$ and $\text{Cu}_2\text{MnSnS}_4$, obtained at the PBE level (Table 1) and compare to published crystal structures. XRD (X-ray diffraction) analysis by Brockway dating back to 1934 revealed that natural $\text{Cu}_2\text{FeSnS}_4$ samples crystallise in ST structure [28]. Those results were subsequently confirmed in the 1970s by Ganiel et al., they furthermore studied the magnetic ordering via Mössbauer spectroscopy and found that it was anti-ferromagnetic [29]. In 1972 Springer studied the solution series $\text{Cu}_2\text{Fe}_{1-x}\text{Zn}_x\text{SnS}_4$. Beyond $x = 0.4$ and above 680°C he observed an ST crystal structure he labeled $\beta\text{-Cu}_2(\text{Fe}/\text{Zn})\text{SnS}_4$. Below $x = 0.4$ and 680°C he found another tetragonal phase he labeled $\alpha\text{-Cu}_2(\text{Fe}/\text{Zn})\text{SnS}_4$ [25,30]. In 2000 pure $\alpha\text{-Cu}_2\text{FeSnS}_4$ was synthesised [26]. After the solid state reaction of CuFeS_2 on SnS at 1323 K in sealed graphite crucible for 24 h the product was cooled slowly over 50 h. Through the slow cooling they obtained the thermodynamically most stable α -phase. Through XRD measurements the space group of the sample was determined to be $P\bar{4}$ [26]. Those results were confirmed by Rincon et al. who furthermore studied the magnetic susceptibility and revealed that also $\alpha\text{-Cu}_2\text{FeSnS}_4$ exhibits an anti-ferromagnetic ordering [27].

Table 1. Optimized lattice parameter a and c (in Å) for $\text{Cu}_2\text{FeSnS}_4$ ST $P\bar{4}$ and KS at the PBE level of theory in comparison to experimental (exp.) lattice parameter. The first column refers to the magnetic phase, ΔE denotes the energy difference to the most stable phase (in meV) and μ_{Fe} refers to the magnitude of the magnetic moment at Fe (in μ_B).

Mag.	ST				$P\bar{4}$				KS	Method
	a	c	μ_{Fe}	ΔE	a	c	μ_{Fe}	ΔE	ΔE	
AM	5.471	10.695	3.1	22	5.469	5.346	3.1	0	122	PBE
FM	5.467	10.724	3.1	82	5.469	5.365	3.1	152	139	PBE
AM	5.460	10.742			5.433	5.410				Exp. [27,29]

Our PBE results for $\text{Cu}_2\text{FeSnS}_4$ agree very well with the experiments. We found the anti-ferromagnetic $P\bar{4}$ (corresponding to $\alpha\text{-Cu}_2\text{FeSnS}_4$) structure to be most stable (Table 1). But it is only 22 meV more stable than the naturally occurring anti-ferromagnetic ST structure. The anti-ferromagnetic KS structure is another 100 meV above the anti-ferromagnetic ST structure. The small energy difference between ST and $P\bar{4}$ may give an explanation why the $P\bar{4}$ phase is hard to obtain in pure form. From the experimental results we conclude that the formation of the ST phase has to be kinetically favoured. This aspect dominates the crystallisation process if the samples are rapidly cooled. We expect the thermodynamic equilibrium to build up slowly based on the small energy difference between the $P\bar{4}$ and ST structures, hence slow cooling is crucial to obtain $\alpha\text{-Cu}_2\text{FeSnS}_4$. In agreement with the experimental data we find the anti-ferromagnetic ordering favoured over the ferromagnetic ordering by 82 meV and 152 meV, for ST and $P\bar{4}$, respectively. The PBE lattice parameter for both $\text{Cu}_2\text{FeSnS}_4$ phases agree reasonably well with the XRD experiments. The lattice parameters change only slightly between the magnetic phases and are within the error bars of the functional applied.

Our PBE prediction for the most stable structure for $\text{Cu}_2\text{MnSnS}_4$ does not agree with experimental results. Magnetisation and neutron-diffraction measurements have shown that $\text{Cu}_2\text{MnSnS}_4$ has an anti-ferromagnetic ST structure [31]. We predict the anti-ferromagnetic KS structure to be 35 meV more stable (Table 2). We also tested the $P\bar{4}$ structure and found it to be the least stable anti-ferromagnetic and ferromagnetic structure. The anti-ferromagnetic $P\bar{4}$ structure is 17 meV less stable than the anti-ferromagnetic ST phase at the PBE level. Our results on the relative KS and ST stability agree closely with PBEsol calculations by Scragg et al [32]. The same group has also carried out HSE06 calculations and found the ST structure to be more stable than the KS structure. The difference is only 15 meV per unit cell. The error in the lattice constants of the PBE calculations is in the range of the differences between the structures and magnetic phases. The PBE lattice constants for $\text{Cu}_2\text{MnSnS}_4$ show subtle interplay between magnetism and structure but all of them are close to the experimental lattice parameter of ST (AM).

Table 2. Optimized lattice parameter a and c (in Å) for $\text{Cu}_2\text{MnSnS}_4$ KS, ST and $P\bar{4}$ at the PBE level of theory in comparison to other simulated and experimental (exp.) lattice parameter. The first column refers to the magnetic phase, ΔE denotes the energy difference to the most stable phase (in meV) and μ_{Mn} refers to the magnitude of the magnetic moment at Mn (in μ_B).

Mag.	ST				KS				$P\bar{4}$	Method
	a	c	μ_{Mn}	ΔE	a	c	μ_{Mn}	ΔE	ΔE	
AM	5.498	10.895	4.1	35	5.468	11.020	4.1	0	52	PBE
FM	5.504	10.880	4.1	49	5.477	11.000	4.2	39	87	PBE
AM	5.407	10.678	4.0	37	5.369	10.832	4.0	0		PBEsol [32]
AM	5.519	10.795	4.5	0	5.468	11.038	4.4	15		HSE06 [32]
AM	5.517	10.806								Exp. [31]

In contrast to the KS equilibrium structure of $\text{Cu}_2\text{ZnSnS}_4$, the compounds $\text{Cu}_2\text{FeSnS}_4$ and $\text{Cu}_2\text{MnSnS}_4$ experimentally favour a ST and/or $P\bar{4}$ structure. The ST and $P\bar{4}$ structures are group theoretically related, both structures exhibit similar cationic layers. We can rationalise the formation of ST and or $P\bar{4}$ structures over KS by comparing the ionic crystal radii (defined according to Fumi and Tosi [33]) of the substituted bivalent elements (Zn, Fe and Mn) in chalcogenides determined by Shannon [34].

$\text{Cu}_2\text{ZnSnS}_4$ in the KS structure consists of $\text{Cu}^+\text{-Zn}^{2+}$ layers and $\text{Cu}^+\text{-Sn}^{4+}$ layers. The crystal radius of Zn^{2+} ($r_c = 0.60$ Å) is identical to the crystal radius of Cu^+ ($r_c = 0.60$ Å), which allows them to fit in the same layer. If we replace Zn^{2+} with the larger Fe^{2+} ($r_c = 0.63$ Å) or Mn^{2+} ($r_c = 0.66$ Å), a ST or $P\bar{4}$ structure is formed. In those structures pure Cu^+ layers alternate with $\text{Sn}^{4+}\text{-Fe}^{2+}/\text{Mn}^{2+}$ layers. Like this the largest and the smallest ion (Sn^{4+} , $r_c = 0.55$ Å) are paired in one layer. In a KS structure the large bivalent cation would have

to be in the same layer as the second largest Cu^+ ion. We suspect that this is the main reason which drives the formation of the ST and/or $P\bar{4}$ structures for the magnetic derivatives.

In contrast to $\text{Cu}_2\text{FeSnS}_4$, we do not find the ST structure to be more stable than KS in our calculations for $\text{Cu}_2\text{MnSnS}_4$, although Mn^{2+} has an even larger ionic crystal radius than Fe^{2+} . We found that PBE fails to describe the electron density around Mn^{2+} , the charge is more smeared out than for Fe^{2+} which leads to larger positive charge at Mn (for details see Table A3 in Appendix A.1).

The PBE lattice parameter a and c of the ST and $P\bar{4}$ structure ($2c$ for the $P\bar{4}$ structure) for $\text{Cu}_2\text{FeSnS}_4$ differ by less than 0.1 %. The differences in $\text{Cu}_2\text{MnSnS}_4$ of a and c between ST and KS are larger, particularly in c where the difference is 2 %. We think that the reason must be the different composition of the cationic layers. If we compare the ST structures of both materials, we find that the size of the lattice parameters corresponds to the crystal radius of the bivalent cation. All presented structures for $\text{Cu}_2\text{FeSnS}_4$ and $\text{Cu}_2\text{MnSnS}_4$ have lattice parameter within 2 % of the values for the $\text{Cu}_2\text{MnSnS}_4$ KS (5.485 Å and 10.94 Å [23]).

3.2. Pressure-Dependent Enthalpies

If we plot and compare the enthalpies for $\text{Cu}_2\text{FeSnS}_4$ (Figure 2a,b) we find the anti-ferromagnetic $P\bar{4}$ structure to be most stable up to 16.3 GPa. Throughout this pressure range the anti-ferromagnetic ST structures is only 22 to 40 meV less stable. The anti-ferromagnetic KS structure is even less stable than the ferromagnetic ST structure which is about 100 meV above the $P\bar{4}$ structure. The energy splitting between AM and FM increases from the KS over the ST to the $P\bar{4}$ structure. As a consequence the ferromagnetic $P\bar{4}$ structure is as unstable as the ferromagnetic KS structure in the investigated pressure range. At 16.3 GPa, we find a transition from the $P\bar{4}$ structure to the GeSb structure. Its purely a structural transition, the magnetic phase remains anti-ferromagnetic. The cell volume decreases by 13% (Table 3) through the transition. At 23.0 GPa we predict a magnetic phase transition of GeSb to ferromagnetic. The energy difference between the two different magnetic phases is very small, at the structural transition pressure it is 15 meV and decreases up to the magnetic transition pressure. Afterwards it increases again, but the difference remains small, at 25 GPa it amounts to 75 meV. The anti-ferromagnetic modification for KS and ST is more stable than the ferromagnetic modification over the whole pressure range. As pointed out for the equilibrium structures, the anti-ferromagnetic $P\bar{4}$ structure and the ST structure can be observed experimentally, depending on the preparation method. Due to the small energy difference between both structures also at the transition pressure, we predict that an ST-to-GeSb transition would also appear at a very similar pressure as the $P\bar{4}$ -to-GeSb transition.

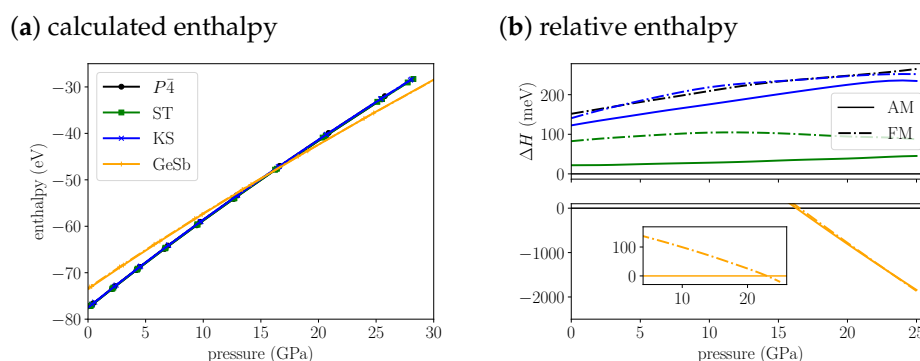


Figure 2. (a) The calculated enthalpies of $\text{Cu}_2\text{FeSnS}_4$ $P\bar{4}$, ST, KS and GeSb structural models as a function of pressure. Because the enthalpy differences are very small we plot the (b) relative enthalpy with reference to most stable low pressure structure $P\bar{4}$ on the right. The top plot shows all low pressure structures, the bottom plot the high pressure GeSb structure. The insert in the bottom shows the energy difference of the FM to the AM structure for GeSb. For the anti-ferromagnetic structures, we use solid lines and for the ferromagnetic structures we use dash-dotted lines.

Table 3. Predicted transitions for $\text{Cu}_2\text{FeSnS}_4$ and $\text{Cu}_2\text{MnSnS}_4$ in comparison to experimental transition for $\text{Cu}_2\text{ZnSnS}_4$. The table contains the transition pressure (p_T in GPa) with the corresponding cell volumina before (V_1 in \AA^3) and after (V_2 in \AA^3) the transition, ΔV denotes the relative volume change. All volumina refer to two formula units.

Composition	p_T	Transition	V_1	V_2	ΔV
$\text{Cu}_2\text{FeSnS}_4$	16.3	$P\bar{4}(\text{AM}) \rightarrow \text{GeSb}(\text{AM})$	272	236	−13.1%
$\text{Cu}_2\text{FeSnS}_4$	23.0	$\text{GeSb}(\text{AM}) \rightarrow \text{GeSb}(\text{FM})$	226	225	−0.6%
$\text{Cu}_2\text{MnSnS}_4$	12.1	$\text{KS}(\text{AM}) \rightarrow \text{GeSb}(\text{FM})$	289	248	−14.0%
$\text{Cu}_2\text{ZnSnS}_4$ [6]	16.0	$\text{KS} \rightarrow \text{GeSb}$	280	240	−15.2%

The enthalpy for $\text{Cu}_2\text{MnSnS}_4$ (Figure 3a,b) indicates that anti-ferromagnetic KS is most stable at ambient conditions and up to 12.1 GPa, where we predict a KS-to-GeSb phase transition. The structural phase transition is accompanied by a magnetic phase transition from anti-ferromagnetic to ferromagnetic. The cell volume decreases by 14% (Table 3) through the transition. At the transition pressure the ferromagnetic GeSb modification is 66 meV more stable than the anti-ferromagnetic modification. With increasing pressure the difference is nearly constant, at 20 GPa it amounts to 73 meV. For the KS structure the anti-ferromagnetic modification remains more stable than the ferromagnetic modification by over 40 meV throughout the whole pressure range. For the ST structure the ferromagnetic modification becomes more stable around 12 GPa. The difference between both magnetic phases is much lower than for KS and remains below 20 meV throughout the whole pressure range. The anti-ferromagnetic $P\bar{4}$ has a very similar stability as the ferromagnetic ST structure. The splitting between AM and FM is the largest, rendering the ferromagnetic $P\bar{4}$ structure the least stable through the whole pressure range. As pointed out above, the relative stability of KS and ST is wrong at the PBE level. Over the whole pressure range the difference in energy between KS and ST stays below 50 meV. In comparison to the energy change induced by the structural phase transition (already 1 eV at 5 GPa above phase transition), this energy difference is small. That is why we think we can still predict a phase transition around 12 GPa. But experimentally we expect a ST(AM)-to-GeSb(FM) transition instead of the KS-to-GeSb phase transition our calculations suggest.

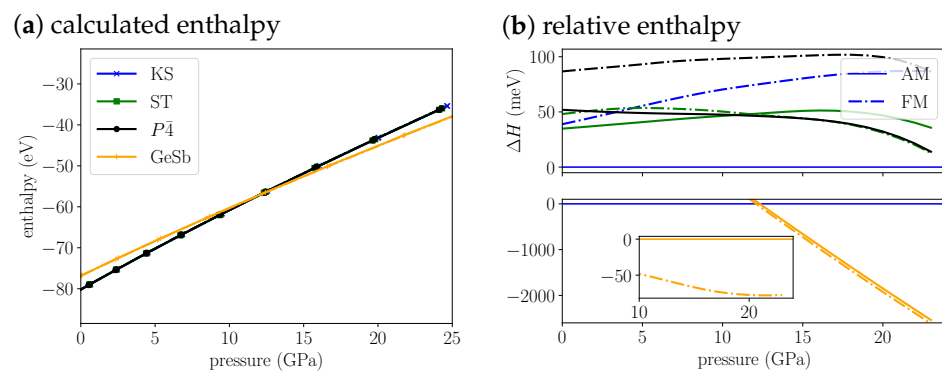


Figure 3. (a) The calculated enthalpies of $\text{Cu}_2\text{MnSnS}_4$ KS, ST, $P\bar{4}$ and GeSb structural models as a function of pressure. Because the enthalpy differences are very small we plot the (b) relative enthalpy with reference to most stable low pressure KS structure on the right. The top plot shows all low pressure structures, the bottom plot the high pressure GeSb structure. The insert in the bottom shows the energy difference of the FM to the AM structure for GeSb. For the anti-ferromagnetic structures we use solid lines and for the ferromagnetic structures we use dash dotted lines.

3.3. Electronic Structure

We investigated the electronic band structure for equilibrium and high-pressure structures for both compounds at the equilibrium and at the transition pressure with the HSE06 hybrid functional [17].

For $\text{Cu}_2\text{FeSnS}_4$, we predicted the band gap of the anti-ferromagnetic ST structure to be 1.3 eV (Table 4). Based on absorption spectra, the band gap was determined to be 1.6 eV [35]. We think that the difference from our prediction is largely due to the fact that we only optimised our structures at the PBE level but also partly due to the error of the HSE06 functional in reproducing band gaps. In an earlier study within our group we obtained similar results for $\text{Cu}_2\text{ZnSnS}_4$ KS. Experimentally the $\text{Cu}_2\text{ZnSnS}_4$ KS band gap is determined to be 1.5 eV [6]. The HSE06 band gap for the PBE optimised structure is 1.2 eV. Only if the structure is also optimised at the HSE06 level, we obtain the experimental band gap [36]. The HSE06 band gap deviation for $\text{Cu}_2\text{ZnSnS}_4$ of the PBE structure is -0.3 eV. We expect it to have similar magnitude for $\text{Cu}_2\text{FeSnS}_4$ and $\text{Cu}_2\text{MnSnS}_4$.

Table 4. Calculated HSE06 band gaps (in eV) for $\text{Cu}_2\text{FeSnS}_4$ and $\text{Cu}_2\text{MnSnS}_4$ for KS and ST structural models (struc.) in comparison to experimental (exp.) results. For DOS plots please refer to Appendix A.4.1.

Composition	Struc.	AM	FM	Exp. (AM)
$\text{Cu}_2\text{FeSnS}_4$	$P\bar{4}$	1.0	0.8	-
$\text{Cu}_2\text{FeSnS}_4$	ST	1.3	0.9	1.6 eV [35]
$\text{Cu}_2\text{MnSnS}_4$	KS	1.3	1.0	-
$\text{Cu}_2\text{MnSnS}_4$	ST	1.1	1.0	1.42–1.79 eV [32]

The HSE06 band gap for the most stable anti-ferromagnetic $P\bar{4}$ structure of $\text{Cu}_2\text{FeSnS}_4$ is 1 eV. For $P\bar{4}$ and ST $\text{Cu}_2\text{FeSnS}_4$ the anti-ferromagnetic modification has an 0.2 and 0.3 eV larger band gap than the ferromagnetic modification.

For $\text{Cu}_2\text{MnSnS}_4$ we predicted an equilibrium band gap for ST of 1.1 eV (Table 4). Experimental measurements by Raudsich et al. of $\text{Cu}_2\text{MnSnS}_4$ indicate a band gap of 1.42 to 1.79 eV. All measured samples contained $\text{Cu}_2\text{MnSn}_3\text{S}_8$ as a secondary phase. They also calculated the band gap at the HSE06 level which they reported to be 1.5 eV. Again the deviation to our result must be due to the fact that they also carried out the optimisation at the HSE06 level while we restricted ourselves to PBE optimisations.

To understand the change of the electronic structures under pressure, we also calculated the DOS at the transition pressures for both systems. For the $P\bar{4}$ structure of $\text{Cu}_2\text{FeSnS}_4$ at the transition pressure the band gap is widened to 1.4 eV (Figure 4). For the naturally occurring ST structure (AM) the band gap is widened to 1.5 eV (for DOS see Appendix A.4.2). After the transition to the anti-ferromagnetic GeSb structure the band gap closes completely. In the DOS plot for anti-ferromagnetic GeSb at the transition pressure we can see that all bands from the valence band now extend in the region from 0 eV to 1.5 eV which is the band gap region for the $P\bar{4}$ structure. Thus we predict a change from semi-conducting to metallic behaviour. The band gap stays zero with the second magnetic transition from anti-ferromagnetic to ferromagnetic.

For $\text{Cu}_2\text{MnSnS}_4$ we find the same behaviour concerning the electronic structure at the transition pressure, a closing of the gap and a metallic character above the transition pressure (Figure 4). During the structural transition, the magnetic structure changes from AM to FM. We are confident that this also holds for the ST (AM) to GeSb (FM) transition we expect based on the observation that the experimental equilibrium structure for $\text{Cu}_2\text{MnSnS}_4$ is the anti-ferromagnetic ST structure. To verify this assumption we also calculated the DOS for ST at the transition pressure, its band gap is 1.2 eV (for DOS see Appendix A.4.2). This confirms that also for the ST (AM) to GeSb (FM) transition the electronic structure would change from semi-conducting to metallic.

Both materials show similar electronic structure changes at the transition pressure as $\text{Cu}_2\text{ZnSnS}_4$, which changes from semi-conducting to metallic at 16 GPa (for details see Appendix A.4.2).

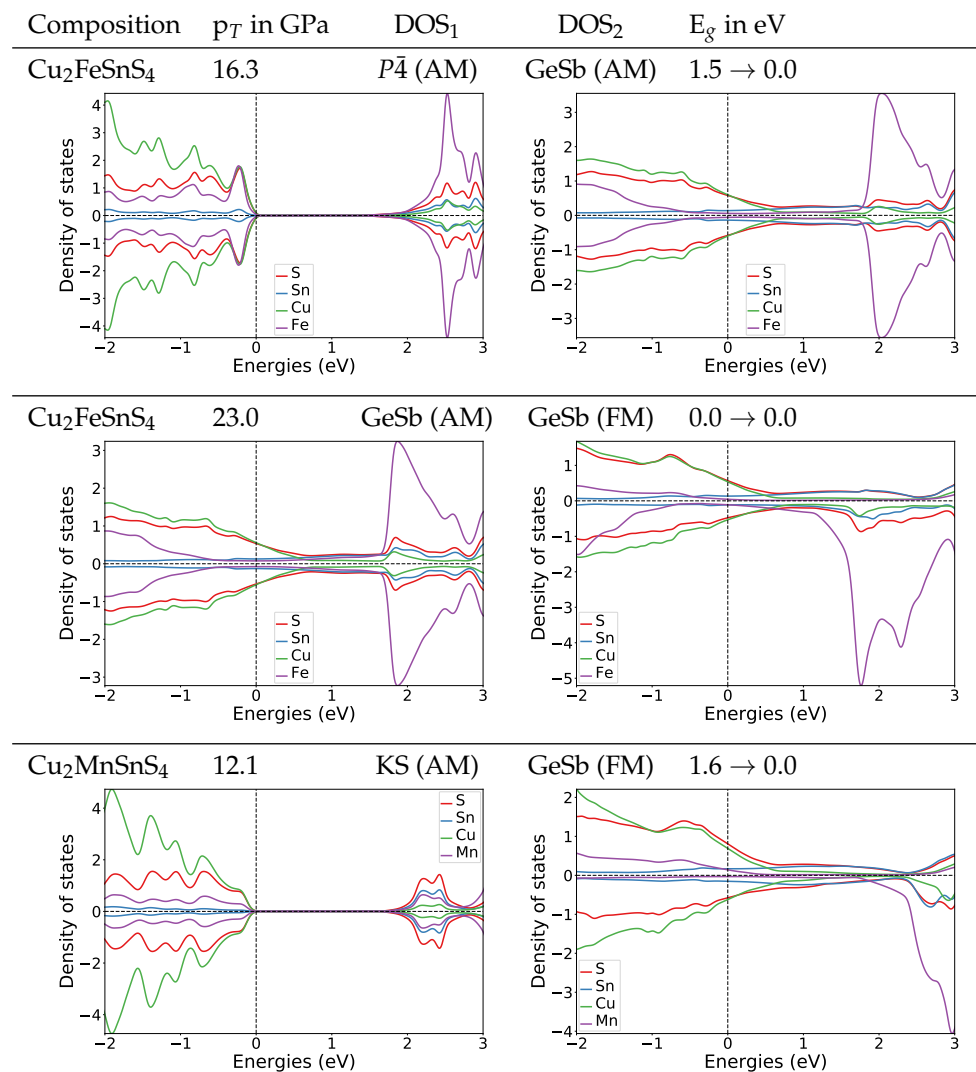


Figure 4. DOS plots at the transition pressure at the HSE06 level for the listed pressure induced transitions for $\text{Cu}_2\text{FeSnS}_4$ and $\text{Cu}_2\text{MnSnS}_4$.

3.4. Mechanical Properties

Finally we want to analyse how the bulk modulus changes due to the phase transitions in the magnetic materials $\text{Cu}_2\text{FeSnS}_4$ and $\text{Cu}_2\text{MnSnS}_4$ and compare to $\text{Cu}_2\text{ZnSnS}_4$. In the used equation of states the equilibrium volume, the bulk modulus and its pressure dependence are fit parameters.

First of all it strikes that regardless of the composition all tetragonal anti-ferromagnetic structures (KS, ST or $P\bar{4}$) have very similar bulk moduli ranging within 2 GPa around the value for $\text{Cu}_2\text{ZnSnS}_4$ KS (Table 5). The first derivative B'_0 shows larger differences, the values for $\text{Cu}_2\text{FeSnS}_4$ and $\text{Cu}_2\text{MnSnS}_4$ are 7 % and 10 % lower than for the KS $\text{Cu}_2\text{ZnSnS}_4$ material. Without an error analysis we can not determine whether the differences in B'_0 are significant. At zero pressure the $P\bar{4}$ (AM) structure of $\text{Cu}_2\text{FeSnS}_4$ has a higher bulk modulus than the ST (AM) structure, but at higher pressures eventually it flips due to the larger first derivative for the ST (AM) structure. If we compare the same structure ST(AM) for all three materials, the bulk modulus of Mn over Zn to Fe are slightly increasing, but only in a range where it would not be measurable experimentally.

Table 5. PBE bulk modulus (B_0 in GPa) and first derivative (B'_0 in GPa/m³) for the listed structural models (Struc.) with the given magnetic phase (Mag.) for the listed compositions. Derived from the Birch–Murnaghan EoS fit. For all fit parameters please refer to Appendix A.3.

Composition	Struc. (Mag.)	B_0	B'_0
Cu ₂ FeSnS ₄	$P\bar{4}$ (AM)	68.32	4.38
Cu ₂ FeSnS ₄	ST (AM)	69.24	4.27
Cu ₂ FeSnS ₄	GeSb (AM)	85.77	3.84
Cu ₂ FeSnS ₄	GeSb (FM)	80.38	4.25
Cu ₂ MnSnS ₄	ST (AM)	67.25	4.16
Cu ₂ MnSnS ₄	GeSb (AM)	80.49	3.83
Cu ₂ ZnSnS ₄ [6]	KS	68.63	4.64
Cu ₂ ZnSnS ₄ [6]	ST	68.77	4.64
Cu ₂ ZnSnS ₄ [6]	GeSb	82.16	4.57

All bulk moduli for the anti-ferromagnetic GeSb structures are in the range of 77.8–85.8 GPa, thus each about 15 % larger than their tetragonal counterparts. In all cases the phase transition leads to stiffer materials. The bulk modulus of GeSb is smallest for Cu₂MnSnS₄ (AM), followed by Cu₂ZnSnS₄ and largest for Cu₂FeSnS₄ (AM). This is the same ordering we observe for the ST (AM) phases.

4. Conclusions

We calculated first principle enthalpies with PBE for different structural models for Cu₂FeSnS₄ and Cu₂MnSnS₄ to identify low and high-pressure modifications. Thereby, we probed ferromagnetic and anti-ferromagnetic phases.

In agreement with experimental findings, we found the anti-ferromagnetic $P\bar{4}$ structure to be the most stable for Cu₂FeSnS₄ at ambient pressure. We additionally confirmed that the naturally occurring ST (AM) is nearly as stable until the following transition. At 16.3 GPa, we predict a structural transition to the anti-ferromagnetic GeSb structure, thereby, the coordination number of the metal ions changes from 4 to 6. The structural transition is accompanied by a change of the electronic structure from semi-conducting to metallic. At 23.0 GPa, we found a magnetic phase transition from anti-ferromagnetic to ferromagnetic, the electronic structure remains metallic.

Due to the deficits of the used density functional, we failed to identify the correct equilibrium structure for Cu₂MnSnS₄. All possible low pressure phases are in a small energy window, and PBE predicts the KS (AM) structure as most stable. Experimental data and HSE06 optimisations indicate that anti-ferromagnetic ST structure is present under ambient conditions. At the HSE06 level the difference is only 15 meV per unit cell [32], and also at the PBE level the difference is small (under 50 meV over the whole pressure range). All four-fold coordinated anti-ferromagnetic structures show a structural and magnetic phase transition to GeSb (FM) around 12 GPa. This transition also leads to a change of the electronic structure from semi-conducting to metallic.

The results for both materials are similar to our findings for Cu₂ZnSnS₄, where we observe a KS-to-GeSb transition around 16 GPa [6]. Also in Cu₂ZnSnS₄ this transition leads to a change of the electronic structure from semi-conducting to metallic. Only taking into account the band gaps and the predicted transition pressures, we conclude that the magnetic material Cu₂FeSnS₄ is similarly suited for the use in thin film solar cells as Cu₂ZnSnS₄. Cu₂MnSnS₄ also has a band gap in the desired range for a solar cell absorber but is less resistant against tensile stress than Cu₂ZnSnS₄ and Cu₂FeSnS₄.

Author Contributions: Conceptualization, E.M.H., B.P. and T.K.; methodology, T.K.; investigation, M.G. and T.K.; writing—original draft preparation, T.K.; writing—review and editing, E.M.H., B.P. and T.K.; supervision, B.P. All authors have read and agreed to the published version of the manuscript.

Funding: This research was funded by Deutsche Forschungsgemeinschaft (DFG) grant number PA1360/14-1 (Beate Paulus) and LE781/19-1 (Martin Lerch, TU Berlin).

Acknowledgments: The authors acknowledge the North-German Supercomputing Alliance (HLRN) for providing HPC (high performance computing) resources that have contributed to the research results reported in this paper. Financial support from International MaxPlanck Research School (IMPRS) Functional Interfaces in Physics and Chemistry is gratefully acknowledged. We thank Martin Lerch (TU Berlin) and Ilias Efthymiopoulos (GFZ Potsdam) for useful discussion.

Conflicts of Interest: The authors declare no conflict of interest.

Abbreviations

The following abbreviations are used in this manuscript:

DFT	density functional theory
KS	kesterite
ST	stannite
AM	anti-ferromagnetic
FM	ferromagnetic
XRD	x-ray diffraction
DOS	density of states

Appendix A.

Appendix A.1. Equilibrium Optimisations

To understand why PBE predicts the correct stability of the equilibrium structures for $\text{Cu}_2\text{FeSnS}_4$ but not for $\text{Cu}_2\text{MnSnS}_4$ we calculated the Bader charges [37] at the PBE (fully optimised) and HSE06 level (only single point calculation on top of PBE structure) for anti-ferromagnetic KS and ST (Table A3).

We can see that for both materials and structures PBE assigns about $0.2 e^-$ less electron density than HSE06 to Fe or Mn ions. If we look closer we can see that the difference for Mn is slightly smaller than for Fe. It is -0.16 and $-0.17 e^-$ for KS and ST respectively, while it is $-0.19 e^-$ for Fe in KS and ST. That means that in PBE the charge is a little more smeared out with reference to the HSE06 charge in $\text{Cu}_2\text{MnSnS}_4$ compared to $\text{Cu}_2\text{FeSnS}_4$. We suspect that this is the reason for the stabilisation of KS over ST at the PBE level.

Table A1. Optimized lattice parameter a and c (in Å) for $\text{Cu}_2\text{FeSnS}_4$ for the listed structural (Struc.) models and magnetic (Mag.) phases at the PBE level of theory. μ_{Fe} refers to the magnitude of the magnetic moment at Fe (in μ_B) and E_{tot} denotes the total energy (in eV). For GeSb and $P\bar{4}$ the length of $2c$ is listed for better comparison.

Struc.	Mag.	a	c	μ_{Fe}	E_{tot}
KS	AM	5.417	10.943	3.1	−77.507740
KS	FM	5.424	10.930	3.1	−77.490464
ST	AM	5.471	10.695	3.1	−77.607942
ST	FM	5.467	10.724	3.1	−77.547627
GeSb	AM	5.160	10.220	3.3	−73.495692
GeSb	FM	5.152	10.214	3.3	−73.336453
$P\bar{4}$	AM	5.469	5.346	3.1	−77.629895
$P\bar{4}$	FM	5.469	5.365	3.1	−77.478290

Table A2. Optimized lattice parameter a and c (in Å) for $\text{Cu}_2\text{MnSnS}_4$ for the listed structural (Struc.) models and magnetic (Mag.) phases at the PBE level of theory. μ_{Mn} refers to the magnitude of the magnetic moment at Mn (in μ_B) and E_{tot} denotes the total energy (in eV). For GeSb and $P\bar{4}$ the length of $2c$ is listed for better comparison.

Struc.	Mag.	a	c	μ_{Mn}	E_{tot}
KS	AM	5.468	11.020	4.1	−80.227182
KS	FM	5.477	11.000	4.2	−80.188168
ST	AM	5.498	10.895	4.1	−80.192347
ST	FM	5.504	10.880	4.1	−80.178549
GeSb	AM	5.212	10.257	4.2	−76.819659
GeSb	FM	5.219	10.233	4.2	−76.844830
$P\bar{4}$	AM	5.504	10.875	4.1	−80.175182
$P\bar{4}$	FM	5.509	10.869	4.1	−80.139990

Table A3. Bader charges for B=Fe or Mn (in e^-) the listed anti-ferromagnetic Cu_2BSnS_4 structures at the PBE and HSE06 level.

Struc	$Q_{\text{PBE}}(\text{Fe})$	$Q_{\text{HSE06}}(\text{Fe})$	$Q_{\text{PBE}}(\text{Mn})$	$Q_{\text{HSE06}}(\text{Mn})$
KS	0.86	1.05	1.02	1.18
ST	0.86	1.05	1.02	1.19

Appendix A.2. Volume Scan Data

Table A4. Optimized lattice parameter a and c (in Å) for $\text{Cu}_2\text{FeSnS}_4$ for the listed structural (Struc.) models and magnetic (Mag.) phases with the given volume V (in Å³) at the PBE level of theory. μ_{Fe} refers to the magnitude of the magnetic moment at Fe (in μ_B) and E_{tot} denotes the total energy (in eV). For GeSb and $P\bar{4}$ the length of $2c$ is listed for better comparison.

Struc.	Mag.	V	a	c	μ_{Fe}	E_{tot}
KS	FM	252	4.962	10.236	2.1	−72.500085
KS	FM	256	4.987	10.292	2.3	−73.162308
KS	FM	264	5.074	10.253	2.6	−74.310555
KS	FM	272	5.130	10.335	2.7	−75.241648
KS	FM	280	5.180	10.435	2.8	−75.971945
KS	FM	288	5.229	10.532	2.9	−76.533331
KS	FM	296	5.278	10.624	3.0	−76.951155
KS	FM	304	5.323	10.728	3.0	−77.238280
KS	FM	312	5.370	10.820	3.1	−77.411308
KS	FM	320	5.415	10.913	3.1	−77.485911
KS	FM	328	5.459	11.007	3.2	−77.474309
KS	AM	252	4.835	10.780	2.1	−72.534384
KS	AM	256	4.922	10.568	2.4	−73.180529
KS	AM	264	5.041	10.391	2.6	−74.330969
KS	AM	272	5.097	10.469	2.7	−75.270313
KS	AM	280	5.149	10.560	2.8	−76.010711
KS	AM	288	5.205	10.629	2.9	−76.576505
KS	AM	296	5.260	10.699	2.9	−76.990092
KS	AM	304	5.313	10.768	3.0	−77.271416
KS	AM	312	5.363	10.849	3.0	−77.438253
KS	AM	320	5.409	10.936	3.1	−77.506327
KS	AM	328	5.451	11.041	3.1	−77.488117
ST	FM	252	5.241	9.173	2.3	−72.677371
ST	FM	256	5.215	9.414	2.4	−73.327281
ST	FM	264	5.199	9.767	2.6	−74.465043
ST	FM	272	5.222	9.975	2.6	−75.378350
ST	FM	280	5.266	10.099	2.7	−76.096158
ST	FM	288	5.298	10.260	2.8	−76.646269

Table A4. Cont.

Struc.	Mag.	V	a	c	μ_{Fe}	E_{tot}
ST	FM	296	5.344	10.366	2.9	-77.050457
ST	FM	304	5.382	10.494	3.0	-77.323902
ST	FM	312	5.420	10.621	3.0	-77.484475
ST	FM	320	5.465	10.716	3.1	-77.547280
ST	FM	328	5.506	10.818	3.1	-77.524008
ST	AM	252	5.234	9.199	2.5	-72.705087
ST	AM	256	5.175	9.558	2.5	-73.368579
ST	AM	264	5.194	9.787	2.6	-74.519354
ST	AM	272	5.220	9.983	2.7	-75.443729
ST	AM	280	5.266	10.098	2.8	-76.170060
ST	AM	288	5.302	10.245	2.9	-76.722183
ST	AM	296	5.343	10.370	2.9	-77.123752
ST	AM	304	5.383	10.493	3.0	-77.394100
ST	AM	312	5.426	10.596	3.0	-77.551400
ST	AM	320	5.470	10.695	3.1	-77.608948
ST	AM	328	5.511	10.800	3.1	-77.581690
GeSb	FM	184	4.514	9.029	1.1	-59.042973
GeSb	FM	192	4.580	9.153	1.4	-62.359016
GeSb	FM	200	4.642	9.280	1.9	-65.031484
GeSb	FM	208	4.702	9.408	2.2	-67.212811
GeSb	FM	216	4.760	9.534	2.4	-68.932449
GeSb	FM	224	4.820	9.644	2.6	-70.279432
GeSb	FM	232	4.884	9.727	2.8	-71.334858
GeSb	FM	240	4.942	9.827	2.9	-72.126728
GeSb	FM	248	4.998	9.928	3.0	-72.691063
GeSb	FM	256	5.050	10.039	3.1	-73.063012
GeSb	FM	264	5.106	10.128	3.2	-73.270306
GeSb	FM	272	5.158	10.222	3.3	-73.338263
GeSb	FM	280	5.211	10.313	3.3	-73.289486
GeSb	AM	184	4.511	9.041	0.8	-58.970006
GeSb	AM	192	4.571	9.188	1.3	-62.263692
GeSb	AM	200	4.633	9.317	1.9	-64.937380
GeSb	AM	208	4.693	9.444	2.2	-67.109096
GeSb	AM	216	4.756	9.550	2.6	-68.847037
GeSb	AM	224	4.819	9.644	2.8	-70.264357
GeSb	AM	232	4.879	9.745	3.0	-71.369644
GeSb	AM	240	4.934	9.857	3.0	-72.199768
GeSb	AM	248	4.991	9.957	3.1	-72.793709
GeSb	AM	256	5.045	10.057	3.2	-73.188975
GeSb	AM	264	5.102	10.142	3.2	-73.414898
GeSb	AM	272	5.160	10.214	3.3	-73.497756
GeSb	AM	280	5.217	10.287	3.3	-73.458151
$P\bar{4}$	FM	256	5.170	9.576	2.5	-73.146081
$P\bar{4}$	FM	264	5.174	9.863	2.6	-74.308897
$P\bar{4}$	FM	272	5.208	10.029	2.7	-75.241113
$P\bar{4}$	FM	280	5.246	10.174	2.8	-75.976529
$P\bar{4}$	FM	288	5.299	10.256	2.9	-76.542992
$P\bar{4}$	FM	296	5.337	10.390	3.0	-76.958577
$P\bar{4}$	FM	304	5.379	10.508	3.0	-77.240473
$P\bar{4}$	FM	312	5.419	10.625	3.1	-77.408891
$P\bar{4}$	FM	320	5.464	10.720	3.1	-77.476946
$P\bar{4}$	FM	328	5.500	10.845	3.2	-77.458815
$P\bar{4}$	AM	256	5.180	9.541	2.5	-73.413979
$P\bar{4}$	AM	264	5.195	9.781	2.6	-74.558793
$P\bar{4}$	AM	272	5.232	9.935	2.7	-75.479036
$P\bar{4}$	AM	280	5.268	10.089	2.8	-76.200728
$P\bar{4}$	AM	288	5.308	10.222	2.8	-76.750054
$P\bar{4}$	AM	296	5.346	10.356	2.9	-77.149666
$P\bar{4}$	AM	304	5.387	10.475	3.0	-77.417917

Table A4. Cont.

Struc.	Mag.	V	a	c	μ_{Fe}	E_{tot}
$P\bar{4}$	AM	312	5.428	10.589	3.0	−77.573576
$P\bar{4}$	AM	320	5.471	10.692	3.1	−77.630834
$P\bar{4}$	AM	328	5.513	10.793	3.1	−77.602124

Table A5. Optimized lattice parameter a and c (in Å) for $\text{Cu}_2\text{MnSnS}_4$ for the listed structural (Struc.) models and magnetic (Mag.) phases with the given volume V (in Å³) at the PBE level of theory. μ_{Mn} refers to the magnitude of the magnetic moment at Mn (in μ_B) and E_{tot} denotes the total energy (in eV). For GeSb and $P\bar{4}$ the length of $2c$ is listed for better comparison.

Struc.	Mag.	V	a	c	μ_{Fe}	E_{tot}
KS	FM	264	5.038	10.401	3.7	−75.971271
KS	FM	272	5.105	10.436	3.8	−77.081763
KS	FM	280	5.164	10.499	3.9	−77.981251
KS	FM	288	5.230	10.529	3.9	−78.694907
KS	FM	296	5.269	10.660	4.0	−79.244321
KS	FM	304	5.324	10.724	4.0	−79.651541
KS	FM	312	5.373	10.807	4.1	−79.933439
KS	FM	320	5.419	10.896	4.1	−80.106005
KS	FM	328	5.464	10.984	4.2	−80.182458
KS	FM	336	5.507	11.078	4.2	−80.175399
KS	FM	344	5.552	11.161	4.2	−80.094993
KS	AM	264	5.074	10.253	3.7	−76.056793
KS	AM	272	5.116	10.391	3.8	−77.168405
KS	AM	280	5.164	10.501	3.8	−78.063375
KS	AM	288	5.222	10.560	3.9	−78.770453
KS	AM	296	5.273	10.645	4.0	−79.313325
KS	AM	304	5.321	10.737	4.0	−79.712814
KS	AM	312	5.368	10.827	4.0	−79.987024
KS	AM	320	5.414	10.916	4.1	−80.152623
KS	AM	328	5.460	11.004	4.1	−80.223251
KS	AM	336	5.504	11.092	4.2	−80.211358
KS	AM	344	5.548	11.176	4.2	−80.127053
ST	FM	264	5.221	9.686	3.5	−76.055292
ST	FM	272	5.237	9.919	3.6	−77.136314
ST	FM	280	5.255	10.141	3.8	−78.020462
ST	FM	288	5.276	10.346	3.8	−78.723375
ST	FM	296	5.320	10.459	3.9	−79.262214
ST	FM	304	5.365	10.563	4.0	−79.659735
ST	FM	312	5.409	10.662	4.0	−79.933493
ST	FM	320	5.451	10.768	4.1	−80.100813
ST	FM	328	5.495	10.862	4.1	−80.174170
ST	FM	336	5.539	10.953	4.2	−80.164939
ST	FM	344	5.582	11.042	4.2	−80.082896
ST	AM	264	5.214	9.710	3.6	−76.028974
ST	AM	272	5.205	10.039	3.7	−77.121388
ST	AM	280	5.216	10.292	3.8	−78.012122
ST	AM	288	5.264	10.394	3.9	−78.721774
ST	AM	296	5.312	10.491	4.0	−79.267491
ST	AM	304	5.359	10.586	4.0	−79.669937
ST	AM	312	5.404	10.684	4.1	−79.947016
ST	AM	320	5.449	10.779	4.1	−80.115031
ST	AM	328	5.491	10.880	4.1	−80.187778
ST	AM	336	5.536	10.963	4.2	−80.177580
ST	AM	344	5.579	11.053	4.2	−80.094369
GeSb	FM	216	4.767	9.504	3.4	−71.302760
GeSb	FM	224	4.826	9.617	3.6	−72.849469

Table A5. Cont.

Struc.	Mag.	V	a	c	μ_{Fe}	E_{tot}
GeSb	FM	232	4.885	9.723	3.8	−74.086520
GeSb	FM	240	4.943	9.823	3.9	−75.037627
GeSb	FM	248	5.001	9.915	4.0	−75.752127
GeSb	FM	256	5.058	10.007	4.1	−76.266470
GeSb	FM	264	5.119	10.076	4.2	−76.604701
GeSb	FM	272	5.177	10.150	4.2	−76.791058
GeSb	FM	280	5.232	10.230	4.2	−76.845649
GeSb	FM	288	5.287	10.304	4.3	−76.787515
GeSb	FM	296	5.348	10.350	4.3	−76.637821
GeSb	AM	216	4.771	9.491	3.4	−71.231957
GeSb	AM	224	4.829	9.607	3.6	−72.776707
GeSb	AM	232	4.887	9.716	3.8	−74.008456
GeSb	AM	240	4.946	9.810	3.9	−74.965658
GeSb	AM	248	5.004	9.902	4.0	−75.695172
GeSb	AM	256	5.061	9.994	4.1	−76.222902
GeSb	AM	264	5.114	10.095	4.2	−76.569615
GeSb	AM	272	5.170	10.176	4.2	−76.761513
GeSb	AM	280	5.227	10.246	4.2	−76.821969
GeSb	AM	288	5.280	10.332	4.3	−76.771277
GeSb	AM	296	5.335	10.398	4.3	−76.624795
$P\bar{4}$	FM	264	5.287	9.445	3.6	−75.981567
$P\bar{4}$	FM	272	5.263	9.821	3.7	−77.068527
$P\bar{4}$	FM	280	5.265	10.103	3.8	−77.962110
$P\bar{4}$	FM	288	5.292	10.285	3.9	−78.671028
$P\bar{4}$	FM	296	5.322	10.452	3.9	−79.215593
$P\bar{4}$	FM	304	5.365	10.561	4.0	−79.617279
$P\bar{4}$	FM	312	5.410	10.661	4.0	−79.894688
$P\bar{4}$	FM	320	5.455	10.755	4.1	−80.062845
$P\bar{4}$	FM	328	5.498	10.849	4.1	−80.135739
$P\bar{4}$	FM	336	5.543	10.938	4.2	−80.126035
$P\bar{4}$	FM	344	5.584	11.032	4.2	−80.043805
$P\bar{4}$	AM	264	5.239	9.619	3.6	−76.054431
$P\bar{4}$	AM	272	5.203	10.046	3.7	−77.135339
$P\bar{4}$	AM	280	5.243	10.188	3.8	−78.020440
$P\bar{4}$	AM	288	5.273	10.360	3.9	−78.724283
$P\bar{4}$	AM	296	5.332	10.411	4.0	−79.265565
$P\bar{4}$	AM	304	5.363	10.568	4.0	−79.664384
$P\bar{4}$	AM	312	5.408	10.668	4.0	−79.937791
$P\bar{4}$	AM	320	5.454	10.758	4.1	−80.102366
$P\bar{4}$	AM	328	5.497	10.854	4.1	−80.171729
$P\bar{4}$	AM	336	5.540	10.947	4.2	−80.158528
$P\bar{4}$	AM	344	5.583	11.035	4.2	−80.072614

Appendix A.3. Birch–Murnaghan EoS (Equation of State) Fits

Third-order Birch–Murnaghan isothermal equation of state: [22]

$$E(V) = E_0 + \frac{9V_0B_0}{16} \left\{ \left[\left(\frac{V_0}{V} \right)^{\frac{2}{3}} - 1 \right]^3 B'_0 + \left[\left(\frac{V_0}{V} \right)^{\frac{2}{3}} - 1 \right]^2 \left[6 - 4 \left(\frac{V_0}{V} \right)^{\frac{2}{3}} \right] \right\}.$$

E_0 denotes the energy per unit cell at zero pressure, B_0 the bulk modulus at zero pressure, V_0 the reference volume at zero pressure; B'_0 , pressure derivative of the bulk modulus at zero pressure. The corresponding Birch–Murnaghan pressure function can be calculated as follows:

$$P(V) = -\left(\frac{\delta E}{\delta V}\right)_s$$

$$P(V) = \frac{3B_0}{2} \left[\left(\frac{V_0}{V}\right)^{\frac{7}{3}} - \left(\frac{V_0}{V}\right)^{\frac{5}{3}} \right] \left\{ 1 + \frac{3}{4}(B'_0 - 4) \left[\left(\frac{V_0}{V}\right)^{\frac{2}{3}} - 1 \right] \right\}.$$

Table A6. Fitted parameter for the Birch–Murnaghan EoS for Cu₂FeSnS₄ for the listed structural models (Struc.) with the given magnetic phase (Mag.). E_0 (in eV): energy per unit cell at zero pressure, B_0 (in GPa): bulk modulus at zero pressure, V_0/Z (in Å³): reference volume per f.u. at equilibrium and B'_0 (in GPa/m³): pressure derivative of the bulk modulus at zero pressure. The fit data refers to two formula units.

Struc.	Mag.	E_0	V_0/Z	B_0	B'_0
KS	FM	−77.491344	322.72	67.456	4.185
KS	AM	−77.510909	321.59	71.826	3.847
ST	FM	−77.549611	321.55	68.490	4.149
ST	AM	−77.611052	321.06	69.244	4.275
GeSb	FM	−73.339910	272.51	80.384	4.250
GeSb	AM	−73.502836	273.01	85.772	3.838
$P\bar{4}$	FM	−77.480718	322.08	68.511	4.269
$P\bar{4}$	AM	−77.632049	321.08	68.321	4.379

Table A7. Fitted parameter for the Birch–Murnaghan EoS for Cu₂MnSnS₄ for the listed structural models (Struc.) with the given magnetic phase (Mag.). E_0 (in eV): energy per unit cell at zero pressure, B_0 (in GPa): bulk modulus at zero pressure, V_0/Z (in Å³): reference volume per f.u. at equilibrium and B'_0 (in GPa/m³): pressure derivative of the bulk modulus at zero pressure. The fit data refers to two formula units.

Struc.	Mag.	E_0	V_0/Z	B_0	B'_0
KS	FM	−80.189890	331.21	66.394	4.314
KS	AM	−80.228539	330.71	65.767	4.498
ST	FM	−80.181139	330.91	66.090	4.222
ST	AM	−80.195264	330.81	67.247	4.162
$P\bar{4}$	FM	−80.143613	330.85	67.136	4.158
$P\bar{4}$	AM	−80.178661	330.50	67.642	4.090
GeSb	FM	−76.846699	279.79	79.178	4.059
GeSb	AM	−76.825978	280.21	80.491	3.832

Appendix A.4. Electronic Structures

Appendix A.4.1. Equilibrium DOS

If we compare the equilibrium DOS plots for anti-ferromagnetic ST Cu₂FeSnS₄ and anti-ferromagnetic KS Cu₂MnSnS₄ to their Cu₂ZnSnS₄ counterparts (Figure A1) we can see that the differences are small in the total DOS. In all three materials the valence band is dominated by the Cu 3d and S 3p bands. In the magnetic materials additionally the 3d bands of Fe and Mn contribute significantly to the valence band, but their DOS is much smaller than for Cu and S bands. The conduction band for Cu₂ZnSnS₄ KS and ST is dominated by the Sn 5s and the S 3p bands. In Cu₂FeSnS₄ and Cu₂MnSnS₄ this also holds true. In the magnetic materials additionally the 3d bands of Fe and Mn contribute significantly to the conduction band. The DOS of the $P\bar{4}$ symmetric structure for Cu₂FeSnS₄ looks nearly identical to the ST (AM) DOS, which is not surprising because they have a very similar structure (same cationic layers).

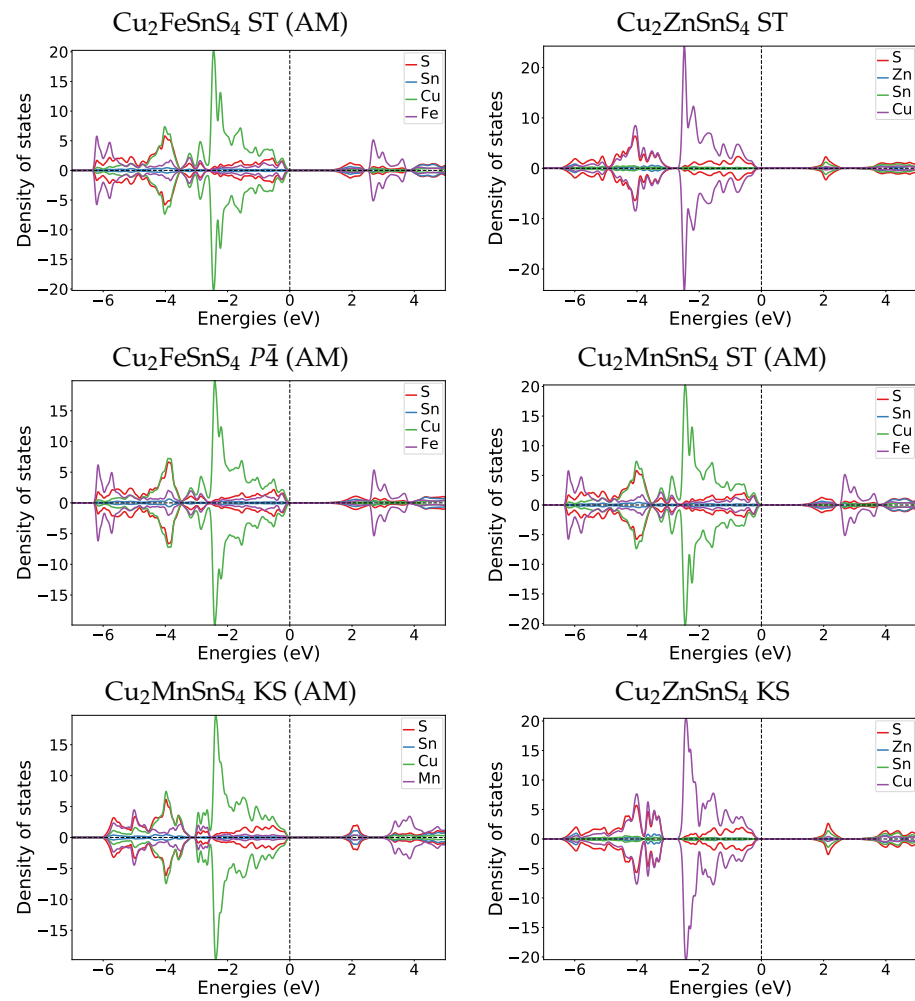


Figure A1. DOS plots at zero pressure at the HSE06 level for the most stable $\text{Cu}_2\text{FeSnS}_4$ and $\text{Cu}_2\text{MnSnS}_4$ structures in comparison to $\text{Cu}_2\text{ZnSnS}_4$ [6] counterparts.

Appendix A.4.2. Transition Pressure DOS

Comparing the DOS of both magnetic materials to their parent $\text{Cu}_2\text{ZnSnS}_4$ KS material DOS (Figure A3), we find that also in $\text{Cu}_2\text{ZnSnS}_4$ the former band gap region (0 to 2 eV) in GeSb consist of the same bands as the valence band. The most striking difference is that in $\text{Cu}_2\text{ZnSnS}_4$ GeSb the former band gap region has two dedicated peaks at 0.6 and 1.6 eV, while in the magnetic cases the DOS amplitude stays relatively constant throughout the whole band gap region.

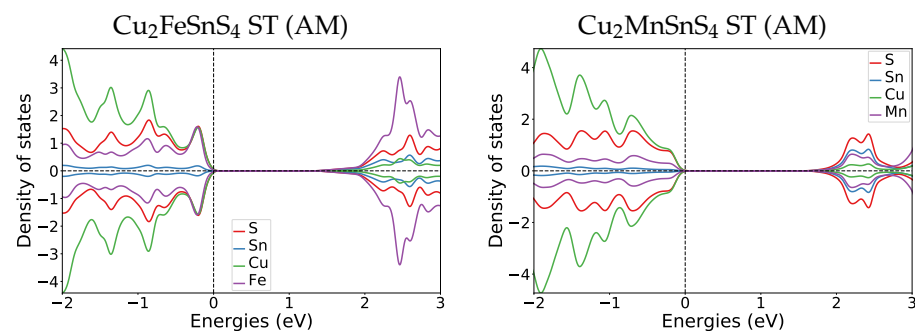


Figure A2. DOS plots at the transition pressure at the HSE06 level for ST $\text{Cu}_2\text{FeSnS}_4$ and $\text{Cu}_2\text{FeSnS}_4$.

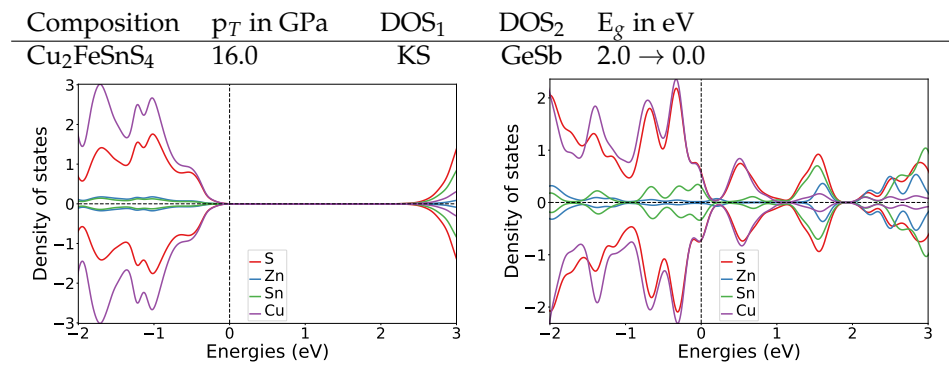


Figure A3. DOS plots at the transition pressure at the HSE06 level for the listed pressure induced transitions for $\text{Cu}_2\text{ZnSnS}_4$ [6].

Appendix A.4.3. Band Gaps

Table A8. Band gaps (E_g in eV) for $\text{Cu}_2\text{FeSnS}_4$ for the listed structural (Struc.) models and magnetic (Mag.) phases with the given volume V (in \AA^3) at the HSE06 level of theory. μ_{Fe} refers to the magnitude of the magnetic moment at Fe (in μ_B) and E_{tot} denotes the total energy (in eV).

Struc.	Mag.	V	E_g	μ_{Fe}	E_{tot}
KS	FM	322	0.9	3.4	−97.133326
KS	AM	321	1.2	3.4	−97.141564
ST	FM	321	0.9	3.4	−97.167788
ST	AM	320	1.3	3.4	−97.059621
GeSb	FM	271	0.0	3.6	−93.312877
GeSb	AM	272	0.0	3.6	−93.393502
$P\bar{4}$	FM	321	0.8	3.5	−97.258338
$P\bar{4}$	AM	320	1.0	3.4	−97.168055
$P\bar{4}$	AM	272	1.4	3.2	−94.755077
GeSb	AM	237	0.0	3.5	−91.816612
GeSb	AM	226	0.0	3.5	−90.500725
GeSb	FM	225	0.0	3.5	−90.160584

Table A9. Band gaps (E_g in eV) for $\text{Cu}_2\text{MnSnS}_4$ for the listed structural (Struc.) models and magnetic (Mag.) phases with the given volume V (in \AA^3) at the HSE06 level of theory. μ_{Mn} refers to the magnitude of the magnetic moment at Mn (in μ_B) and E_{tot} denotes the total energy (in eV).

Struc.	Mag.	V	E_g	μ_{Mn}	E_{tot}
KS	FM	330	1.0	4.4	−101.542001
KS	AM	329	1.3	4.4	−101.528785
ST	FM	330	1.0	4.4	−101.518509
ST	AM	329	1.1	4.4	−101.529370
$P\bar{4}$	FM	330	0.8	4.4	−101.449803
$P\bar{4}$	AM	329	1.0	4.4	−101.490508
GeSb	FM	279	0.0	4.6	−97.670815
GeSb	AM	279	0.0	4.5	−97.702174
KS	AM	288	1.6	4.3	−99.895633
GeSb	FM	248	0.0	4.5	−96.648114
ST	AM	289	1.2	4.3	−99.919608

References

1. Katagiri, H.; Jimbo, K.; Maw, W.S.; Oishi, K.; Yamazaki, M.; Araki, H.; Takeuchi, A. Development of CZTS-based thin film solar cells. *Thin Solid Films* **2009**, *517*, 2455–2460.
2. Liu, X.; Feng, Y.; Cui, H.; Liu, F.; Hao, X.; Conibeer, G.; Mitzi, D.B.; Green, M. The current status and future prospects of kesterite solar cells: A brief review. *Prog. Photovolt. Res. Appl.* **2016**, *24*, 879–898. [[CrossRef](#)]
3. Scragg, J.J.; Dale, P.J.; Peter, L.M.; Zoppi, G.; Forbes, I. New routes to sustainable photovoltaics: Evaluation of $\text{Cu}_2\text{ZnSnS}_4$ as an alternative absorber material. *Phys. Stat. Sol.* **2008**, *245*, 1772–1778. [[CrossRef](#)]
4. Siebentritt, S.; Schorr, S. Kesterites—a challenging material for solar cells. *Prog. Photovolt. Res. Appl.* **2012**, *20*, 512–519. [[CrossRef](#)]
5. Chen, S.; Gong, X.; Walsh, A.; Wei, S.H. Crystal and electronic band structure of $\text{Cu}_2\text{ZnSnX}_4$ ($X = \text{S}$ and Se) photovoltaic absorbers: First-principles insights. *Appl. Phys. Lett.* **2009**, *94*, 041903. [[CrossRef](#)]
6. Efthimiopoulos, I.; Küllmey, T.; Speziale, S.; Pakhomova, A.S.; Quennet, M.; Paulus, B.; Ritscher, A.; Lerch, M.; Koch-Müller, M. Pressure-induced structural and electronic transitions in kesterite-type $\text{Cu}_2\text{ZnSnS}_4$. *J. Appl. Phys.* **2018**, *124*, 085905. [[CrossRef](#)]
7. Quennet, M.; Ritscher, A.; Lerch, M.; Paulus, B. The order-disorder transition in $\text{Cu}_2\text{ZnSnS}_4$: A theoretical and experimental study. *J. Solid State Chem.* **2017**, *250*, 140–144. [[CrossRef](#)]
8. Kresse, G.; Hafner, J. Ab initio molecular dynamics for liquid metals. *Phys. Rev. B* **1993**, *47*, 558–561. [[CrossRef](#)]
9. Kresse, G.; Hafner, J. Ab initio molecular-dynamics simulation of the Liquid–Metal—Amorphous—Semiconductor transition in germanium. *Phys. Rev. B* **1994**, *49*, 14251–14269. [[CrossRef](#)]
10. Kresse, G.; Furthmüller, J. Efficient iterative schemes for ab initio total-energy calculations using a plane-wave basis set. *Phys. Rev. B* **1996**, *54*, 11169–11186. [[CrossRef](#)]
11. Kresse, G.; Furthmüller, J. Efficiency of ab-initio total energy calculations for metals and semiconductors using a plane-wave basis set. *Comput. Mater. Sci.* **1996**, *6*, 15–50. [[CrossRef](#)]
12. Blöchl, P. Projector augmented-wave method. *Phys. Rev. B* **1994**, *50*, 17953–17979. [[CrossRef](#)]
13. Kresse, G.; Joubert, D. From ultrasoft pseudopotentials to the projector augmented-wave method. *Phys. Rev. B* **1999**, *59*, 1758–1775. [[CrossRef](#)]
14. Press, W.H.; Flannery, B.P.; Teukolsky, S.A.; Vetterling, W.T.; Kramer, P.B. Numerical Recipes: The Art of Scientific Computing. *Phys. Today* **1987**, *40*, 120–122. [[CrossRef](#)]
15. Monkhorst, H.J.; Pack, J.D. Special points for Brillouin-zone integrations. *Phys. Rev. B* **1976**, *13*, 5188–5192. [[CrossRef](#)]
16. Perdew, J.P.; Burke, K.; Ernzerhof, M. Generalized Gradient Approximation Made Simple. *Phys. Rev. Lett.* **1996**, *77*, 3865–3868. [[CrossRef](#)] [[PubMed](#)]
17. Heyd, J.; Scuseria, G.E.; Ernzerhof, M. Hybrid functionals based on a screened Coulomb potential. *J. Chem. Phys.* **2003**, *118*, 8207–8215. [[CrossRef](#)]
18. Heyd, J.; Scuseria, G.E. Efficient hybrid density functional calculations in solids: Assessment of the Heyd–Scuseria–Ernzerhof screened Coulomb hybrid functional. *J. Chem. Phys.* **2004**, *121*, 1187–1192. [[CrossRef](#)]
19. Heyd, J.; Scuseria, G.E.; Ernzerhof, M. Erratum: “Hybrid functionals based on a screened Coulomb potential” [*J. Chem. Phys.* **118**, 8207 (2003)]. *J. Chem. Phys.* **2006**, *124*, 219906. [[CrossRef](#)]
20. Krukau, A.V.; Vydrov, O.A.; Izmaylov, A.F.; Scuseria, G.E. Influence of the exchange screening parameter on the performance of screened hybrid functionals. *J. Chem. Phys.* **2006**, *125*, 224106. [[CrossRef](#)] [[PubMed](#)]
21. Blöchl, P.E.; Jepsen, O.; Andersen, O. Improved tetrahedron method for Brillouin-zone integrations. *Phys. Rev. B* **1994**, *49*, 16223–16233. [[CrossRef](#)]
22. Birch, F. Finite Elastic Strain of Cubic Crystals. *Phys. Rev.* **1947**, *71*, 809–824. [[CrossRef](#)]
23. Schorr, S. The crystal structure of kesterite type compounds: A neutron and X-ray diffraction study. *Sol. Energy Mater. Sol. Cells* **2011**, *95*, 1482–1488. [[CrossRef](#)]
24. Chen, S.; Walsh, A.; Luo, Y.; Yang, J.H.; Gong, X.G.; Wei, S.H. Wurtzite-derived polytypes of kesterite and stannite quaternary chalcogenide semiconductors. *Phys. Rev. B Condens. Matter Mater. Phys.* **2010**, *82*, 1–8. [[CrossRef](#)]
25. Kissin, S.A. Reinvestigation of the stannite ($\text{Cu}_2\text{FeSnS}_4$)—Kesterite ($\text{Cu}_2\text{ZnSnS}_4$) pseudobinary system. *Can. Mineral.* **1989**, *27 Pt 4*, 689–697.
26. Llanos, J.; Tapia, M.; Mujica, C.; Oró-Sole, J.; Gómez-Romero, P. A New Structural Modification of Stannite. *Boletín la Soc. Chil. Química* **2000**, *45*, 5–11. [[CrossRef](#)]
27. Rincón, C.; Quintero, M.; Moreno, E.; Power, C.; Quintero, E.; Henao, J.A.; Macías, M.A.; Delgado, G.E.; Tovar, R.; Morocoima, M. X-ray diffraction, Raman spectrum and magnetic susceptibility of the magnetic semiconductor $\text{Cu}_2\text{FeSnS}_4$. *Solid State Commun.* **2011**, *151*, 947–951. [[CrossRef](#)]
28. Brockway, L.O. The Crystal Structure of Stannite, $\text{Cu}_2\text{FeSnS}_4$. *Z. Krist. Cryst. Mater.* **1934**, *89*, 434–441. [[CrossRef](#)]
29. Ganiel, U.; Hermon, E.; Shtrikman, S. Studies of magnetic ordering in $\text{Cu}_2\text{FeSnS}_4$ by Mössbauer spectroscopy. *J. Phys. Chem. Solids* **1972**, *33*, 1873–1878. [[CrossRef](#)]
30. Springer, G. The pseudobinary system $\text{Cu}_2\text{FeSnS}_4$ – $\text{Cu}_2\text{ZnSnS}_4$ and its mineralogical significance. *Can. Mineral.* **1972**, *11*, 535–541.
31. Fries, T.; Shapira, Y.; Palacio, F.; Morón, M.C. Magnetic ordering of the antiferromagnet from magnetization and neutron-scattering measurements. *Phys. Rev. B Condens. Matter Mater. Phys.* **1997**, *56*, 5424–5431. [[CrossRef](#)]

32. Rudisch, K.; Espinosa-García, W.F.; Osorio-Guillén, J.M.; Araujo, C.M.; Platzer-Björkman, C.; Scragg, J.J. Structural and Electronic Properties of $\text{Cu}_2\text{MnSnS}_4$ from Experiment and First-Principles Calculations. *Phys. Status Solidi Basic Res.* **2019**, *256*, 1–10. [[CrossRef](#)]
33. Fumi, F.G.; Tosi, M.P. Ionic sizes and born repulsive parameters in the NaCl-type alkali halides-I. The Huggins-Mayer and Pauling forms. *J. Phys. Chem. Solids* **1964**, *25*, 31–43. [[CrossRef](#)]
34. Shannon, R.D. Revised effective ionic radii and systematic studies of interatomic distances in halides and chalcogenides. *Acta Crystallogr. Sect. A* **1976**, *32*, 751–767. [[CrossRef](#)]
35. Prabhakar, R.R.; Zhenghua, S.; Xin, Z.; Baikie, T.; Woei, L.S.; Shukla, S.; Batabyal, S.K.; Gunawan, O.; Wong, L.H. Photovoltaic effect in earth abundant solution processed $\text{Cu}_2\text{MnSnS}_4$ and $\text{Cu}_2\text{MnSn}(\text{S},\text{Se})_4$ thin films. *Sol. Energy Mater. Sol. Cells* **2016**, *157*, 867–873. [[CrossRef](#)]
36. Quennet, M. First Principles Calculations for the Semiconductor Material Kesterite $\text{Cu}_2\text{ZnSnS}_4$ and Se-containing Derivatives. Ph.D. Thesis, Freie Universität Berlin, Berlin, Germany, 2016.
37. Tang, W.; Sanville, E.; Henkelman, G. A grid-based Bader analysis algorithm without lattice bias. *J. Phys. Condens. Matter* **2009**, *21*. [[CrossRef](#)]